Quiet Sun and Coronal hole in Transition Region

A Thesis

submitted to
Indian Institute of Science Education and Research Pune
in partial fulfilment of the requirements for the
BS-MS Dual Degree Programme

by

Nived.V.N

Indian Institute of Science Education and Research Pune
Dr. Homi Bhabha Road,
Pashan, Pune 411008, INDIA.

May, 2018

Supervisor: Durgesh Tripathi

Certificate

This is to certify that this dissertation entitled Quiet Sun and Coronal hole in Transition region towards the partial fulfilment of the BS-MS dual degree programme at the Indian Institute of Science Education and Research, Pune represents study/work carried out by Nived.V.N Indian Institute of Science Education and Research under the supervision of Dr. Durgesh Tripathi, Associate Professor, Inter-University Centre for Astronomy and Astrophysics (IUCAA) , during the academic year 2017-2018.

Student
Nived.V.N

Supervisor
Dr. Durgesh Tripathi

Committee:
Dr. Durgesh Tripathi
Dr. Prasad Subramanian

Declaration

I hereby declare that the matter embodied in the report entitled Quiet Sun and Coronal hole in Transition region are the results of the work carried out by me at Inter-University Centre for Astronomy and Astrophysics (IUCAA), under the supervision of Dr. Durgesh Tripathi and the same has not been submitted elsewhere for any other degree.

Student
Nived.V.N

Supervisor
Dr. Durgesh Tripathi

Acknowledgements

This thesis and all the research I have done in the past year alongside it has been with the help of several people whom I would like to thank here.

Firstly, I would like to thank Dr Durgesh Tripathi, who has been my guide for the past one year. His guidance helped me in all the time of research and writing of this thesis. He has always supported, motivated and corrected me whenever it was required. I am thankful to have had a guide who gave freedom in terms of many things, as long as the required work was done properly.

I would like to thank Avyarthana Ghosh, who is currently pursuing her doctoral research under the guidance of Dr Durgesh Tripathi. She has been a mentor, whose knowledge about processing and analysing the satellite data has helped me countless number of times.

I would like to thank Dr Ramitendranath Bhattacharyya and Dr Avijeet Prasad, who is a Post Doctoral Fellow at Udaipur Solar Observatory, for helping me to understand various magnetic field extrapolation techniques.

Finally, I want to express my deep gratitude towards my father, mother and sister, who have always supported me and believed in me, whatever choices I make in life. Their constant concern for me has helped me be focused and given me inspiration to work towards my chosen goal.

Contents

List of Figures

List of Tables

Abstract

Coronal images of the Sun reveal the presence of dark region on the solar surface. This region of reduced emissivity is known as coronal holes, and they are surrounded by a region of higher emissivity called quiet Sun. Coronal hole intensity is not significantly reduced in the transition region. Many studies suggested that magnetic field is responsible for the unusual appearance of coronal holes in the transition region. This study aims to understand the properties of the coronal hole and quiet Sun in the transition region. We analysed the coronal hole and quiet Sun using Si IV 1394 Å spectral line observations taken by Interface Region Imaging Spectrograph (IRIS) and compared its intensity, Doppler velocity, and non-thermal width for the region with similar magnetic field strength. We found quiet Sun is brighter in transition region with respect to coronal holes and their non-thermal width and Doppler velocity were similar at these heights.

Magnetic field is a fundamental quantity to understand various phenomenon occurring on the Sun. The magnetic field can only be measured at photospheric height. Thus extrapolation techniques are necessary to calculate and model coronal magnetic field. The extrapolation methods are based on the force-free assumption in Corona, which means the non-magnetic forces like pressure gradient and gravity are neglected. The underlying mathematical problem behind the force-free field, which is the relationship between electrical current and the magnetic field, is non-linear. Thus numerical techniques are necessary to solve this non-linear force-free field. Potential and linear force-free fields are also reviewed in this work, they can be used as the first step to the model corona. These two methods cannot accurately reconstruct the coronal magnetic field because they are derived by linearising the underlying non-linear mathematical problem. Thus nonlinear force-free fields are essential for the modelling. Here we reviewed the non-linear techniques including optimization procedure and Aschwanden's vertical current approximation code. The knowledge of observed loop structure can be used to test the accuracy of these extrapolation methods. The extrapolation techniques shall be applied to the quiet Sun and coronal hole regions to understand the structure of the magnetic field in these regions and their possible effects on the heating shall be studied.

Chapter 1

Introduction

Sun is our closest star, a giant ball of hot plasma which maintains life on earth. It is the ultimate source of energy in the solar system. The solar energy is created in the core of the sun via thermonuclear fusion. The temperature of the core is about 15 million K [1]. The energy generated in the core is then transferred to the surface of the Sun and to the atmosphere. The interior region of the Sun above the core is devided into two based on how the energy is transported in these regions. The layer above the core is known as the radiative zone where the energy is transported from a region of high temperature to low temperature by random walking of the photons [2]. In the convective zone, which is the layer above the radiative zone, energy is transported via convection. So the bubbles of gases which is hotter than the surrounding region will rise, and the gas bubble which is cooler than the surroundings will sink [2]. This process helps to transport energy to the visible surface of the Sun, the Photosphere.

Photosphere is the region we see with our naked eyes. It is the lower part of the solar atmosphere. The photosphere appears in a granular pattern because of the convection developed beneath this layer. Most important feature in the photosphere is the sunspots, where the temperature is lower than the surroundings and appear dark in the intensity images. The layer above the photosphere is the chromosphere, which is the primary supplier of mass and energy to the uppermost atmospheric layer of the Sun (Corona). The temperature in the corona is about a million K. The existence high-temperature corona above cooler atmospheric layer is one of the major Solar Physics problems. The region between chromosphere and corona is known as transition region. Here the temperature and number density of electron shows drastic changes with the height. The temperature increases rapidly and the electron number density decreases sharply with the height [3]. Thus the transition region is very important in understanding the coronal heating problem.

Various phenomenon happening in our closest star sun can be understood using solar spectroscopy. Spectroscopy is one of the brilliant techniques to study every form of matter in the universe. It is the study of the interaction between matter and electromagnetic radiation. Mostly used in astronomy to study stars and other stellar objects. Both the terrestrial based and space-based solar observation technique has helped us to explore solar atmosphere in great

detail. Satellites like Solar and Heliospheric Observatory(SOHO), Hinode, Transition Region and Coronal Explorer (TRACE), Ulysses are used in obtaining the images of the sun in the different wavelength band including optical, Infrared, X-ray, UV. Recent satellite missions such as Interface Region Imaging Spectrograph (IRIS) and Solar Dynamic Observatory (SDO) has improved a lot in the temporal and spatial resolution of the images. Helioseismic Magnetic Imager (HMI) onboard SDO provides the magnetic field map of the Solar photosphere. HMI has much better accuracy and resolution in magnetic field measurement compared to the previous mission Michelson Doppler Imager (MDI) onboard SOHO. High-resolution images obtained by IRIS provides an excellent opportunity to study the transition region. Spectral line intensities of some ions are sensitive to temperature and density of the emitting plasma, by analysing intensity data we can derive the temperature and density map of emitting plasma. It can also provide information about Doppler velocity. All these local plasma parameters along with magnetic field data help to understand the physical condition of Solar atmosphere and various dynamic processes occurring on the Sun.

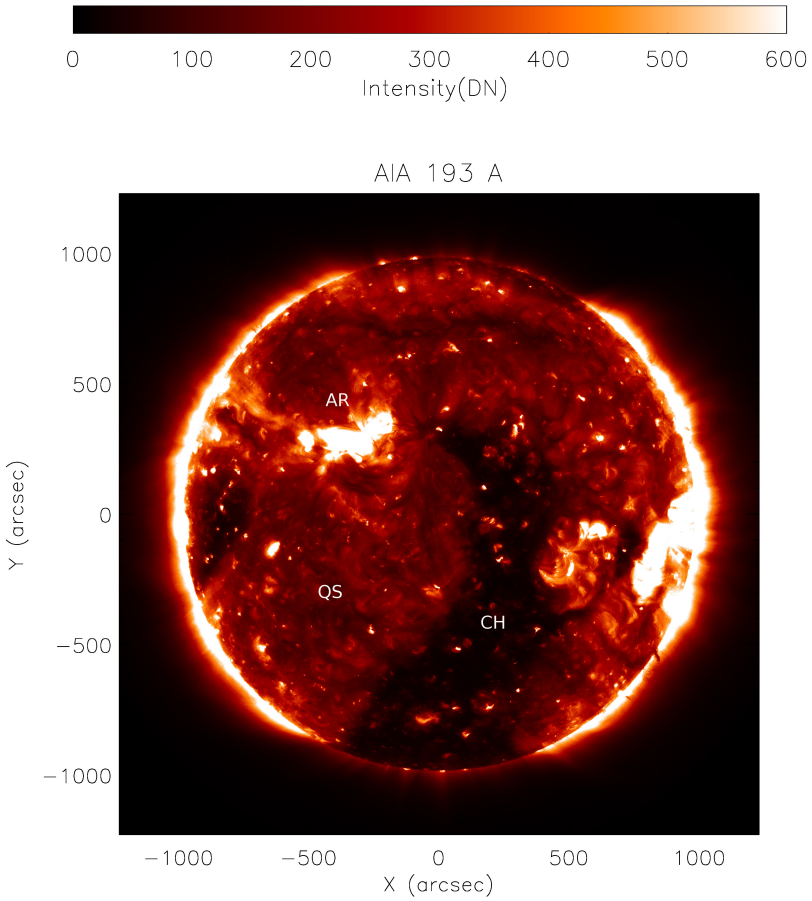

Figure 1.1: Full disk AIA 193 Å image of the Sun.

Figure 1.1 displays the 193 Å channel full disc image of the Sun. This is an extreme ultraviolet image which represents the corona. The bright region represents the Solar active region (AR) where the loop structures are found. These structures are tubes of magnetic field lines. Dynamic processes such as plasma heating, flares, and coronal mass ejection occur in the active region. The dark region in this coronal image is the coronal holes (CH), and it is surrounded by a region of higher emissivity known as quiet Sun (QS). Previous studies suggested that the intensity images of the coronal holes are indistinguishable from the surrounding quiet Sun. If they are distinguishable at coronal height then why not in the transition region? This question needs to be answered. We may be able to solve this problem by studying magnetic field structure in the coronal hole and quiet Sun because the field structures are different in both region. This requires the modelling of magnetic field lines.

The magnetic field modelling is carried out by a different type of extrapolation methods, which uses photospheric magnetogram as the boundary value. All these methods assume that corona is in force-free condition. To solve force-free field, various numerical techniques are necessary because of the non-linearity of the underlying mathematical problem. The numerical technique requires higher computational power, and it is time-consuming compared to analytical methods. Potential and linear force-free field are the simpler versions of the force-free field, they are derived from linearising the non-linear equation. These two force-free fields can be solved easily using analytical methods. But they cannot accurately represent the coronal magnetic field. Thus nonlinear force-free fields are essential for the modelling. Two well-known techniques to solve non-linear force-free field (NLFFF) are the optimization procedure and Aschwanden's non-linear force-free code. The optimization procedure requires the photospheric vector magnetogram to compute NLFFF. Aschwanden code which is based on vertical current approximation only need line of sight magnetogram and observed coronal images to compute NLFFF.

Detailed study of similarities and difference between coronal hole and quiet Sun in transition region are presented in chapter 2, where we analysed their intensity, Doppler velocity and non-thermal width for the region with similar magnetic field strength using Si iv 1394 Å line. In chapter 3 we described three different type of force-free extrapolation methods including potential, linear, and non-linear force-free extrapolation method.

Chapter 2

Quiet Sun and Coronal Hole in Transition Region

2.1 Introduction

Coronal holes (CH) are the dark region (reduced emissivity) on the solar surface at radiation corresponding to the coronal temperature, and they are surrounded by a region of higher emissivity and the weak magnetic field called Quiet sun (QS). At coronal height number density of electron is significantly lower in the coronal hole as compared to the surrounding area [4]. Coronal holes can be observed in a wide range of spectra including UV, X-ray, and Infrared wavelength, they are seen as dark areas on x-ray and EUV images, but they look brighter in He I 1083 nm image [5]. He I 1083 nm absorption line is extremely useful in identifying coronal holes. The advantage of this infrared line is, it can be observed using ground-based telescopes. Coronal Holes are easily distinguishable from surrounding quiet sun and the active region at radiation above $10^6 K$. There are two types of coronal holes, polar coronal holes and equatorial coronal holes. Large Polar coronal holes are present in the southern and northern pole during solar minimum with opposite polarity. As the sun approaches the solar maximum, they become smaller and finally vanish. But during these period isolated coronal holes are observed in lower latitude reaching till equator called equatorial coronal holes.

Magnetic field structures in coronal holes are different from the quiet sun. In coronal holes, a large fraction of field lines are open and extend into interplanetary space [6]. So the hot plasma can escape along the open field lines. But in quiet sun field lines are mainly closed, and the hot gas trapped in the loops radiate, causing the quiet sun to be brighter [7]. Coronal holes are indistinguishable from surrounding quiet sun and the active region at radiation below $6 \times 10^5 K$ [7]. This indicates that at lower transition region and chromosphere coronal holes and quiet Sun look similar.

The present work describes the similarities and difference between coronal holes and quiet sun at lower transition region in Si iv 1394 Å line using the Interface Region Imaging Spectrometer(IRIS). IRIS obtains UV spectra and images in two main pass-bands around 1400Å and 2800Å at high resolution in space(0.33-0.4 arcseconds), time(1s) and spectrally(40 and

CH			QS		
Date of observation	FOV(arcsec)	Exposure time(s)	Date of observation	FOV	Exposure time(s)
2016/12/05	$33'' \times 175''$	30	2016/12/05	$33'' \times 175''$	30
2017/01/03	$33'' \times 175''$	30	2016/12/16	$33'' \times 175''$	30
2017/01/05	$33'' \times 175''$	30	2017/02/05	$33'' \times 175''$	30
2017/01/12	$33'' \times 175''$	30	2017/02/05	$33'' \times 175''$	30
2017/02/05	$33'' \times 175''$	30	2017/02/14	$33'' \times 175''$	30
2017/02/14	$33'' \times 175''$	30	2017/02/14	$33'' \times 175''$	30

Table 2.1: Details of all CH and QS rasters

80mÅ respectively) [8]. High-resolution spectra obtained by IRIS provides us with an excellent opportunity to study the coronal hole and quiet sun in the transition region. In this work we have analysed the intensity, Doppler velocity, non-thermal width of the line Si IV 1394 Å for the region with similar magnetic field strength. Rest of the chapter is structured as follows. The details of the observation and data analysis are presented in section 2.3. In sections 2.4, we have described the observational findings of the present work. Conclusions are outlined in section 2.5.

2.2 Methods

In this study, we have observed six coronal holes and six neighbouring QS using IRIS. All the coronal hole observed in this study are equatorial coronal holes seen within three month period starting from 2016 December to 2017 February. So instrumental degradation does not affect the intensity measurement much. CHs and QS are observed in Si IV 1394 Å emission line. This line is a perfect candidate to study transition region, and its maximum emission temperature (Tmax) is 63000 K [9]. All the IRIS rasters used in this study are dens rasters covering the field of view $33'' \times 175''$ in 96 steps, and the raster cadence is 3044 seconds. The details of all six coronal holes and quiet Sun rasters are shown in table 2.1. The standard SSW routine eis_auto_fit.pro was used to derive integrated spectral line intensities. This routine uses mpfit.pro algorithm to fit single Gaussian to each pixel in the raster.

2.2.1 Identifying Coronal Holes and Quiet sun

Coronal hole rasters contain a small part of quiet Sun also (see figure 2.1). For the analysis, it is important to find out a proper boundary between coronal holes and quiet sun, and this was done by using full disk 193 Å channel image observed by Atmospheric Imaging Assembly on board Solar Dynamic Observatory (SDO). By manual inspection, we defined coronal holes as the region with intensity value less than 50 DN/pix and quiet sun as the region with intensities greater than 50 DN/pix in 193 Å image. To do this, it is mandatory to have a near perfect

co-alignment between IRIS raster and AIA 193 Å image, and this is a difficult task because the images are taken at two different height in solar atmosphere by different instruments. To obtain IRIS-AIA co-alignment, IRIS SJI 1400 Å channel and AIA 1600 Å channels are used, because they both show similar structures due to strong continuum contribution. First, we co-aligned IRIS raster with IRIS Si IV 1400 Å Slit-jaw image (SJI). Co-alignment was performed using standard SSW routine coreg_map.pro and correl_offset.pro. Next, we co-aligned IRIS SJI 1400 Å with AIA 1600 Å image. After that, shift the AIA 193 Å image using the offset obtained with respect to IRIS raster. Co-alignment between IRIS raster and AIA(193Å) channel is shown in figure 2.2 . Figure 2.2(a) displays the Si IV 1394 Å intensity image observed by IRIS on 2017/02/05, and its co-aligned IRIS SJI 1400 Å, AIA 1600 Å, AIA 193 Å intensity images are shown in figure 2.2(b), figure 2.2(c), figure 2.2(d), respectively. White contour in figure 2.2(d) represents the boundary between CH and QS.

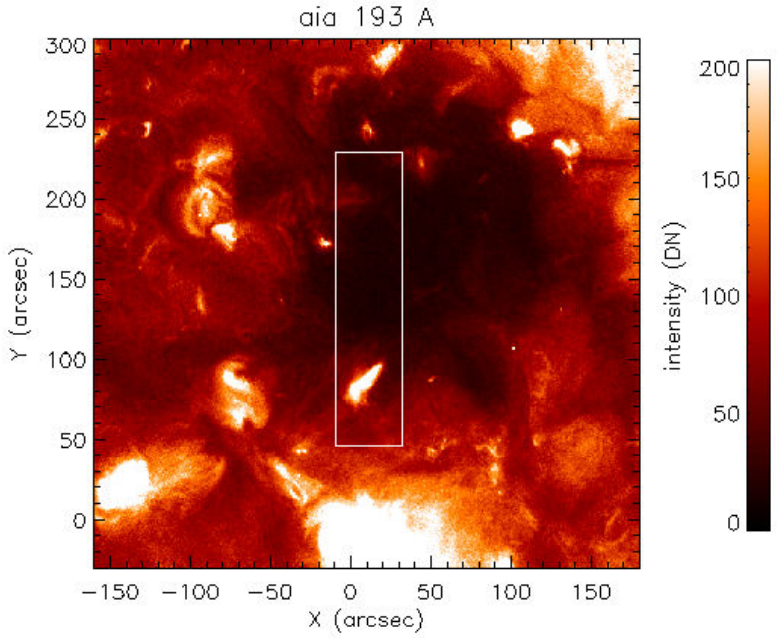

Figure 2.1: Large FOV of AIA 193Å channel image. Over plotted white box represent the rastering area of CH raster observed on 2017/02/05.

2.2.2 Co-aligning IRIS rasters with HMI magnetogram

This project aims to compare the intensities, velocity and non-thermal width derived using Si IV 1394 Å spectral line of coronal holes and quiet sun with its underlying photospheric magnetic field. So we will have an idea about how these quantities behave in QS and CH for the magnetic field with similar strength. To measure magnetic field values at the photosphere, observation recorded with Helioseismic and Magnetic Imager (HMI) onboard SDO is used. To

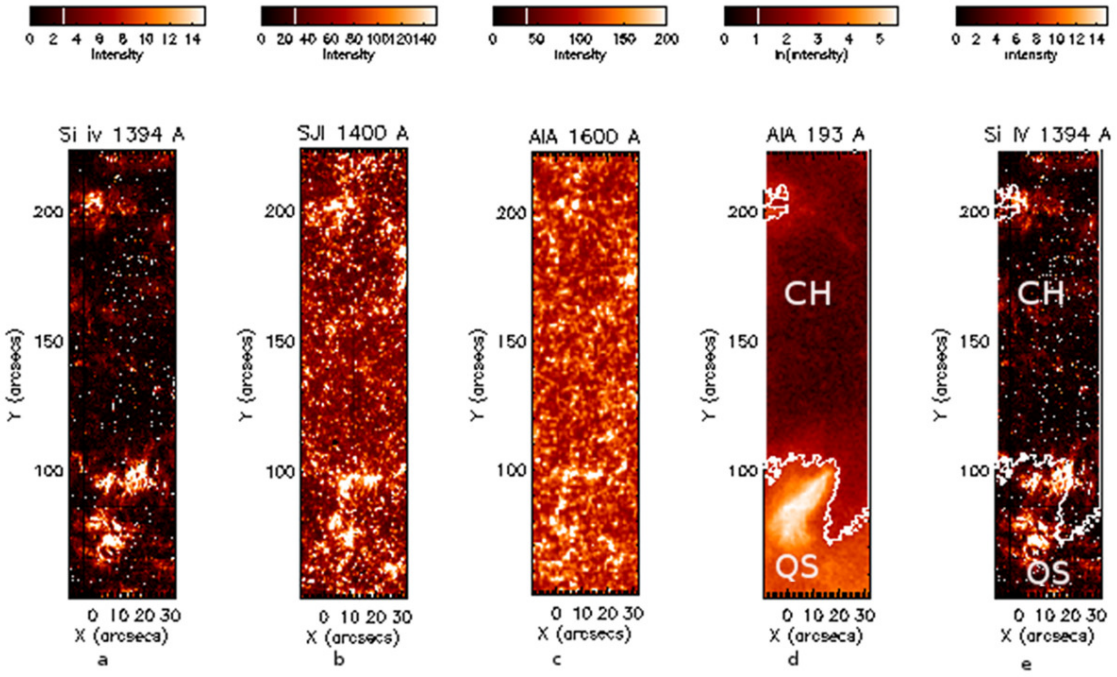

Figure 2.2: Co-aligned IRIS, SJI, AIA images for CH observed on 2017/02/05. (a): IRIS Si IV 1394 intensity image. (b): SJI 1400 Å image corresponding to IRIS raster. (c): AIA 1600 Å channel image corresponding to IRIS raster. (d): AIA 193 Å channel image with white contour showing the boundary of QS and CH. (e): IRIS Si iv 1394 intensity image with over plotted contour, representing the boundary between CH and QS.

compare HMI data with IRIS, we have to have a perfect co-alignment between them. Each raster composed of 96 vertical slices taken at different time. These vertical slices are the one-dimensional array of 548 pixels. HMI full disk magnetograms are available with cadence 45 seconds. All the HMI magnetogram taken during the IRIS rastering period are co-aligned with IRIS intensity image using the help of SJI 1400 Å and AIA 1600 Å channel. Next, we created an artificial raster of HMI by cutting down each vertical slices of HMI magnetogram corresponding to the time and space of IRIS rasters. This is called artificial rastering, an extremely useful technique to compare HMI magnetograms with IRIS rasters. Co-alignment between IRIS raster and HMI images are shown in figure 2.3. Figure 2.3(a) displays the Si IV 1394 Å intensity image observed by IRIS on 2017/02/05, and its co-aligned IRIS SJI 1400 Å, AIA 1600 Å intensity images are shown in figure 2.3(b), figure 2.3(c), respectively. Figure 2.3(d) represents the artificial rasters and co-aligned HMI magnetogram.

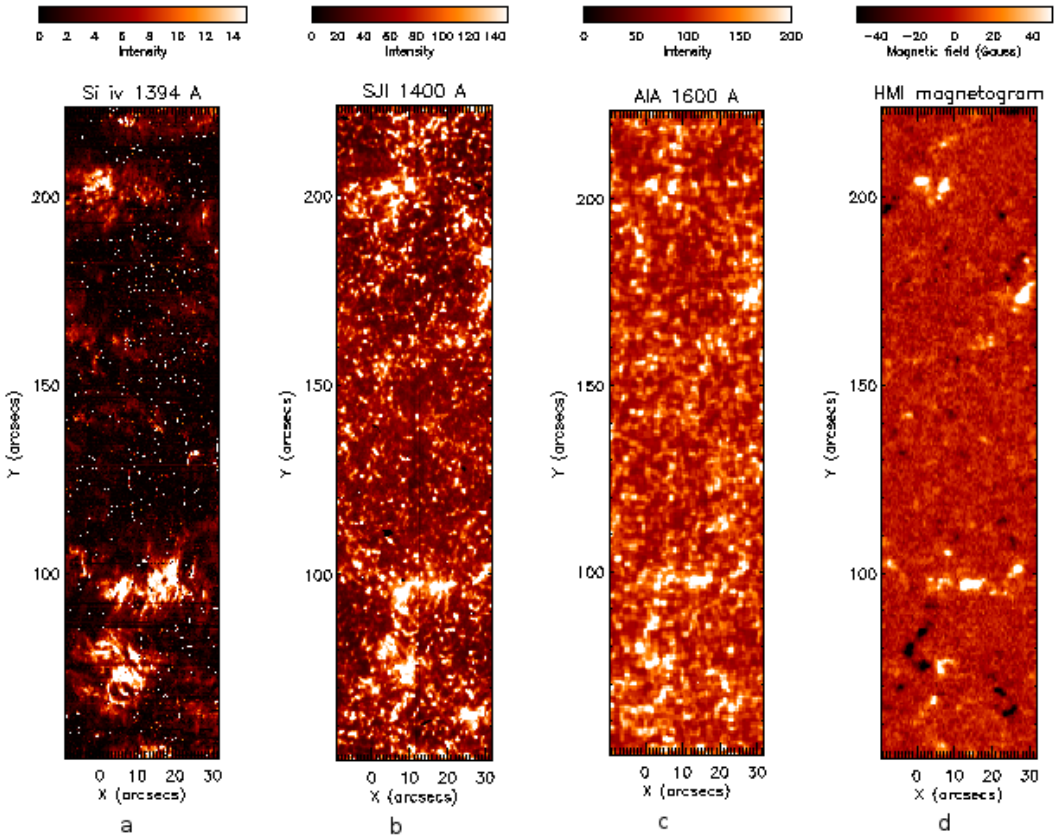

Figure 2.3: IRIS HMI co-alignment using IRIS SJI 1400Å, AIA 1600 Å images

2.2.3 Study of velocity in QS and CH for the region with similar magnetic field strength

Doppler velocities for Si IV 1394 Å line in QS and CH are calculated by using standard SSW routine eis_get_fitdata.pro. Before doing this, we have binned the windata using eis_bin_windata.pro routine. This routine decreases the resolution of the image but helps to reduce error in velocity measurement. Wavelength calibration was done by using Fe II photospheric line. We calculated centroid value λ_{FeII_obs} of the observed wavelength for Fe II line by single Gaussian fitting using well-known mpfit.pro routine. The reference wavelength of Si IV 1394 Å line was calculated using the formula,

$$\lambda_{ref\_SiIV} = \lambda_{SiIV\_lab} - (\lambda_{FeII\_lab-FeII\_obs}) \tag{2.1}$$

λ_{SiIV_lab} is the laboratory wavelength of Si IV 1394 Å line (1393.755 Å)[10] and λ_{FeII_lab} is the laboratory wavelength of Fe II line (1392.817 Å)[10]. Next, we identified the centre of observed Si IV line λ_{SiIV_obs} using the eis_auto_fit procedure. And performed eis_get_fitdata.pro routine to obtain Doppler velocity. This routine uses the formula given below to calculate line of sight

(LOS) velocities.

$$v = \frac{(\lambda_{SiIV\_obs} - \lambda_{ref\_SiIV}) \times c}{\lambda_{ref\_SiIV}}$$

above steps repeated for each QS and CH and compared the velocity in the quiet sun and coronal hole region with very similar magnetic field strength using co-aligned HMI magnetograms.

2.2.4 Study of non-thermal width in QS and CH for the region with similar magnetic field strength

Non-thermal width for Si IV 1394 spectral line in CH and QS are calculated by the formula,

$$\delta\lambda = \frac{\lambda_0}{c}\sqrt{4ln2\left(\frac{2K_BT_i}{m} + \varepsilon^2\right) + \sigma_I^2}$$

Where $\delta\lambda$ is the observed line width, λ_0 is the line centroid (1393.755 Å), K_B is the Boltzmanns constant, T_i is the ion temperature (63000 K), m is the mass of the ion (28.085 u), ε is non-thermal velocity, and σ_I is the instrumental full width half maximum (FWHM). Instrument width is measured in the laboratory before the launch of IRIS mission, which is 31.8 mA [11]. Observed line width ($\delta\lambda$) was calculated using standard SSW routine eis_get_fitdata.pro, which calculates the FWHM width in wavelength unit.

2.3 Results and Discussion

2.3.1 Intensity comparison in CH and QS

Using LOS magnetogram we calculated the radial component of the magnetic field by dividing LOS component of the field by corresponding μ angle, where mu is defined as the cosine of the heliographic longitude. Next we performed a pixel to pixel correlation between Si IV 1394 Å intensity image and the absolute value of radial magnetic field map. This method helps to compare the intensity of CH and QS for the region with similar magnetic field strength. Pixels with LOS magnetic field values less than 10 G are excluded in this calculation because HMI has an error of 10 G [12]. We have excluded higher magnetic field (i.e. more than 80 G) location as those locations were rare and can potentially mislead.

To compare the intensity of Si IV 1394 Å line in CH and QS for the region with similar magnetic field strength, the whole region of QS and CH was divided into various bin based on the strength of the radial magnetic field. If we choose a constant bin size, the number of data points in each bin will decrease with increase in the magnetic field, because locations with

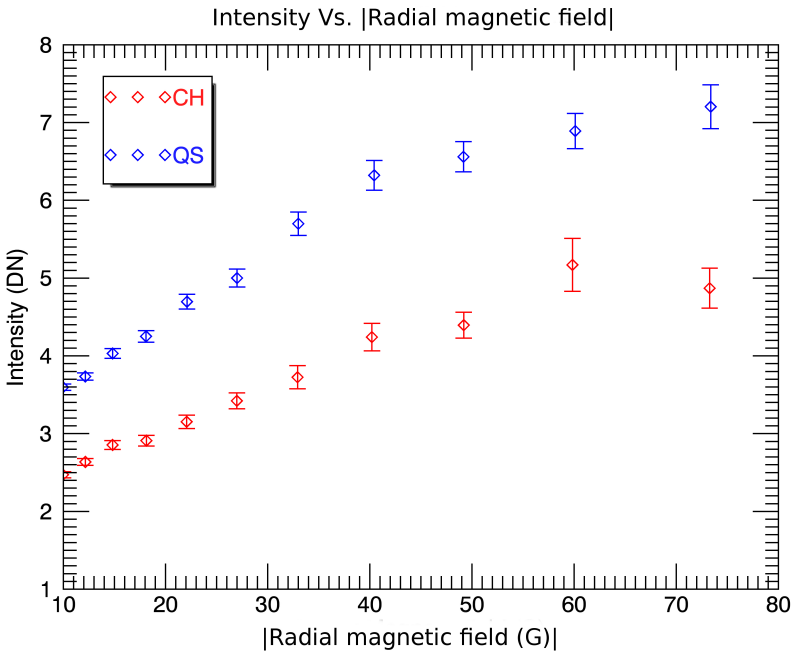

Figure 2.4: Si IV 1394 Å intensity in each magnetic field bin averaged over 6 CH and 6 QS

higher magnetic strength are rare. One way to avoid this problem is to select bin size such that, it increases with the magnetic field. Here we have chosen bin size which increases exponentially with the field. Average intensity and average absolute radial magnetic field are then computed for each magnetic field bin and plotted.

Figure 2.4 displays the average intensity as a function of radial magnetic field bin in six coronal holes and six quiet suns. From the figure, it is clear that QS (blue) intensity in different magnetic field bin are larger than CH (red) intensity, which means the quiet sun is always brighter than the coronal hole for the region with similar magnetic field strength. Also, the intensity difference between CH and QS increases with the magnetic field. Normalised intensity histogram of CH (red) and QS (blue) displayed figure2.6. Intensity bin size chosen here was 0.5 DN. This histogram indicates that for the coronal hole, there is a sharp decrease in the number of pixels as intensity increases as compared to quiet Sun.

These results can be explained by the work of Wiegelmann and Solanki. The large fraction of field line in coronal holes are open, but in the quiet sun, most of the field lines are closed. We have seen that in transition region quiet sun is brighter than coronal holes. The number of long and short loops can be used to explain this result. According to RTV scaling law, long loops are hot and short loops are cool. The number long closed loops that are reaching transition region in coronal holes are lesser compared to the quiet sun, and the short loops are closing down further below the transition region.

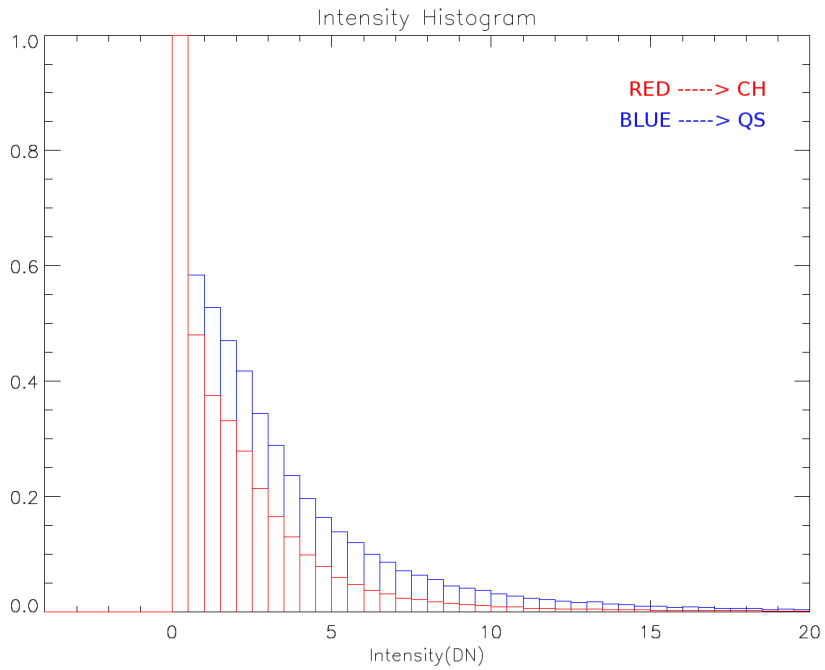

Figure 2.5: Intensity histogram of the coronal hole and quiet Sun

2.3.2 Doppler velocity comparison in CH and QS

The intensity, velocity, LOS magnetic field maps of coronal hole observed on 2017/02/05 are shown in figure 2.6 (a), (b), (c) respectively. The resolution of these images is reduced to decrease the error in Doppler velocity calculation. Figure 2.7 displays the variation of absolute radial velocity with the absolute radial magnetic field in coronal hole and quiet Sun. As mentioned before the radial component of velocity is calculated by dividing LOS velocity by corresponding μ angle. As earlier, the bin size increases exponentially with the magnetic field, to avoid the problem of the lesser number of data points at the higher magnetic field bins. The radial magnetic field below 10G is not plotted because HMI has approximately 10 Gauss error in LOS measurement. This figure shows that radial velocity increases with increasing radial magnetic field strength. The average QS and CH velocities are similar in different magnetic field bins, which means CH and QS velocity for the Si IV 1394Å line are similar for the region with similar magnetic field strength. Larger uncertainty in velocity at the higher magnetic field is due to the lesser number pixel with large magnetic field values.

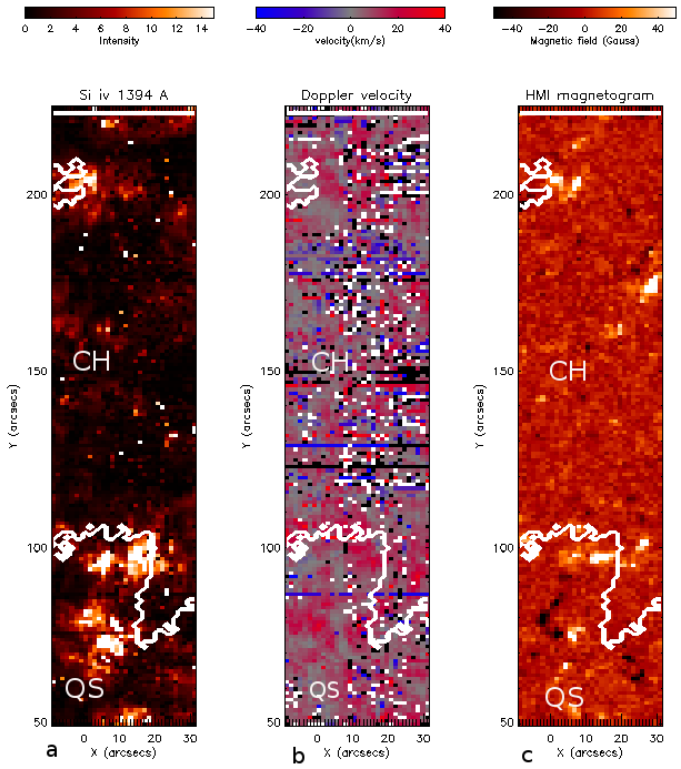

Figure 2.6: Comparison of Si iv 1394 line velocity with magnetic field in CH observed on 2017/02/05. (a): Si IV 1394 Å intensity image. (b): Doppler velocity image of Si IV 1394 Å line. (c): Co-aligned HMI magnetogram. Over plotted white contour on each image represents the boundary between CH and QS.

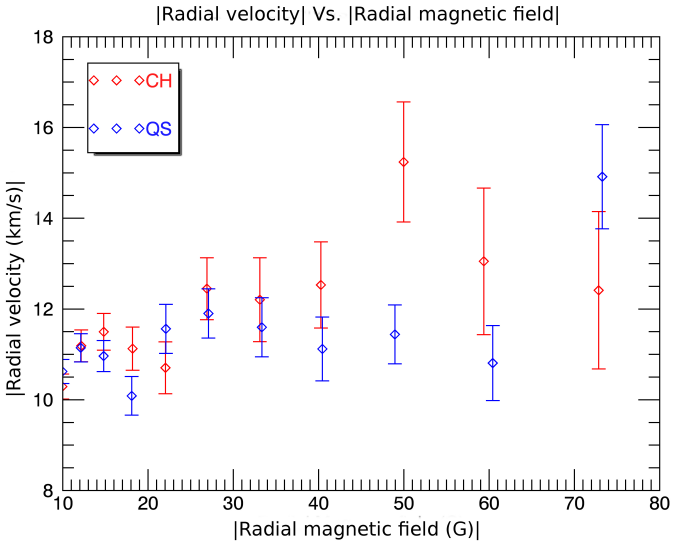

Figure 2.7: Absolute radial velocity in each magnetic field bin averaged over six coronal holes and six quiet Suns

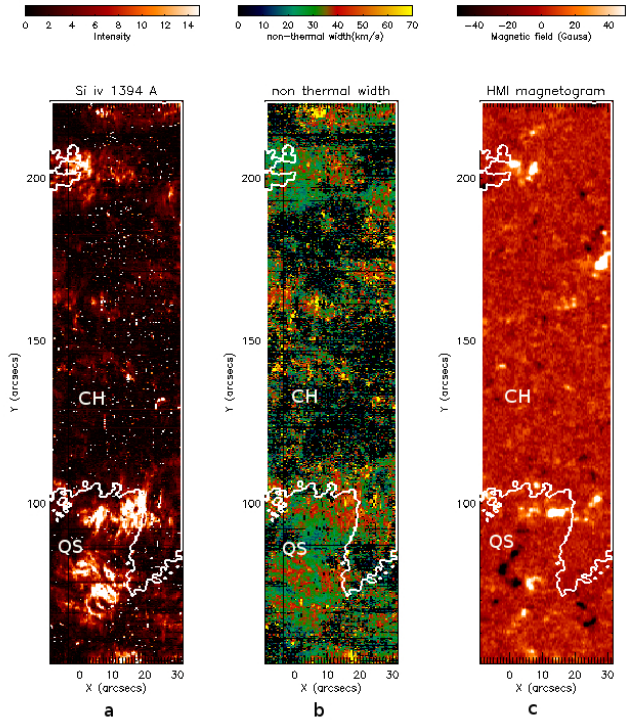

Figure 2.8: Comparison of Si iv 1394 line non-thermal width with magnetic field. (a): Si IV 1394 Å intensity image of a coronal hole observed on 2017/02/05. (b): non-thermal width map of Si IV 1394 Å line. (c): Co-aligned HMI magneto gram. Over plotted white contour on each image represents the boundary between CH and QS.

2.3.3 Non-thermal width comparison in CH and QS

Non-thermal width map of CH observed on 2017/02/05 are shown in figure 2.8. Figure 2.8(a) displays the Si IV 1394 Å intensity IRIS raster, and its corresponding non-thermal width map, co-aligned HMI magnetogram are shown in figure 2.8(b), figure 2.8(c), respectively. Overplotted white contour in each image represents the boundary between CH and QS. From intensity and non-thermal width image, it is clear that there is a good positive correlation between intensity and non-thermal width. Figure 2.9 displays the FWHM non-thermal width in each magnetic field bin averaged over six coronal holes and six quiet suns. The graph shows that non-thermal width increases with increasing magnetic field strength. Here the bin size increases exponentially with the magnetic field, to avoid the problem of the lesser number of data points at the higher magnetic field. The radial magnetic field below 10G is not plotted because HMI has approximately 10 Gauss error in LOS field measurement. The average QS and CH non-thermal width are similar in each magnetic field bins, which means CH and QS non-thermal width for the Si IV 1394Å line are almost equal for the region with similar magnetic field strength. Thus the process that is responsible for non-thermal width is both common in coronal hole and quiet Sun. Larger uncertainty in non-thermal width at the higher magnetic

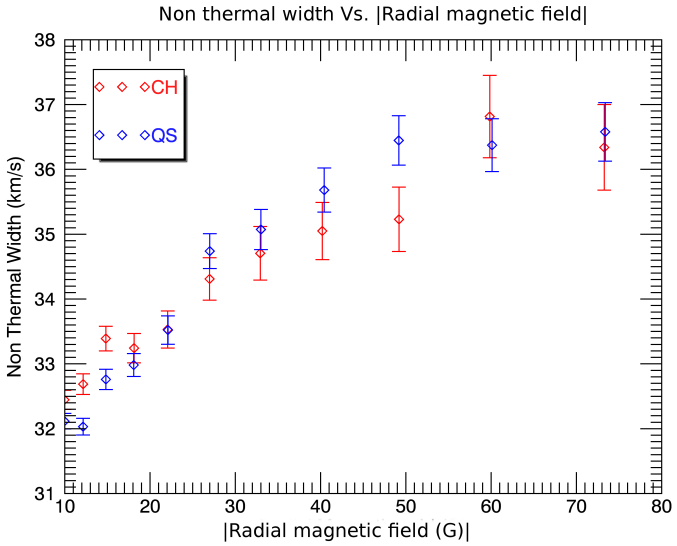

Figure 2.9: Non-thermal width averaged over six coronal holes and six quiet Suns

field is due to the lesser number pixel with large magnetic field values.

2.4 Conclusions

Quiet sun is brighter than coronal holes corresponding to coronal temperature radiation. In the transition region, they look similar. One way to explain this problem is by using the number of short and long loops. According to RTV scaling law, long loops are hot and short loops are cooler. In coronal holes, the number of long-closed loops is lesser compared to the quiet sun. But they have an equal number of short loops. Due to the almost complete absence of closed loops at coronal temperatures in the coronal hole, there is hardly any emission in lines formed at high temperatures [7]. In this study, we found that in transition region the quiet sun is brighter than the coronal hole for the region with similar magnetic field strength. This result can be explained based on the number of long and short closed loops. The number of long loops that are extending till transition region is lesser in the coronal hole compared to quiet Sun, and the short loops are closing down far below the transition region. Thus the quiet Sun is expected to be brighter than the coronal hole even in the transition region. The difference between CH and QS intensity increases with the magnetic field. The non-thermal width and Doppler velocity are almost equal in CH and QS for the region with similar magnetic field strength. So we can conclude that the process that responsible for the non-thermal broadening of the line are common in both QS and CH. A possible reason for such a broadening could be Alfven wave turbulence.

Magnetic field structure in coronal holes and quiet Sun are completely different. By modelling magnetic field structures, we may be able to understand the coronal hole and quiet Sun in great detail. This can be done with the help of various magnetic field extrapolation methods.

Height and length of these field lines can then be calculated, and we can compare how these quantities vary in coronal hole and quiet Sun. To do extrapolation, it is crucial to know the state of the magnetic field in the region of interest. It can be potential, linear force-free, non-linear force-free fields. Detailed theoretical analysis of each extrapolation methods is explained in next chapter.

Chapter 3

Magnetic field Extrapolation

3.1 Introduction

Magnetic field plays an essential role in governing various physical processes occurring in the atmosphere of the Sun. Sun has a complex magnetic topology that continually changes with time, unlike the Earth's simple dipole. Thus, magnetically driven phenomenon, such as solar wind, coronal mass ejection (CME), solar flare, coronal heating and sunspots etc. can only be studied with accurate measurement of magnetic field on the surface and atmosphere of the Sun. The recent mission, Helioseismic Magnetic Imager (HMI) onboard Solar Dynamic Observatory (SDO) provides us high resolution (temporal and spatial) full disk vector magnetograph on the visible surface of the Sun (Photosphere), using Stokes polarimetry technique[13]. The basic technique behind the magnetic field measurement on the Sun's surface is the Zeeman effect, which is the splitting of spectral lines into multiple closely spaced line in the presence of magnetic field, due to the interaction between the magnetic field and the magnetic dipole moment associated with the orbital and spin angular momentum. Unfortunately, these methods are only applicable to the lower atmosphere of the Sun. So we cannot measure the coronal (upper atmosphere) magnetic field using direct methods. One of the reasons behind the difficulty in measurement of coronal magnetic field is the lack of a suitable spectral line. The spectral line with high Landau g factor may not be available at this height, even if there is a line the lower density of corona makes the problem even more difficult, because of the lower intensity of the spectral line. The next problem strength of magnetic field is lesser in corona compared to the photosphere, which makes splitting of spectral line smaller. Another major problem is the temperature of the corona. The temperature of the corona is very high (10^6 K) as compared to the photospheric temperature, which is around 5000 K. Due to the high temperature the thermal width of the spectral line increases and it will reduce the Stokes V signal [14]. The measurement of coronal magnetic field strength is very important to understand the phenomenon such as Solar flare and CMEs in great detail.

The measurement of coronal magnetic field is carried out by a different type of extrapolation methods, which uses photospheric magnetogram as the boundary value. All these methods

assume that corona is in force-free condition ($j \times B = 0$), the proof is given below.

The equation of motion of plasma can be described by,

$$\rho \frac{Dv}{Dt} = -\nabla P + j \times B + \rho g \tag{3.1}$$

Where ρ is the mass density, P is the plasma pressure, $j \times B$ is the Lorentz force. The inertial term can be neglected if the flow speed is smaller compared to Alfven speed, sound speed, and gravitational free-fall speed [15]. Then equation 3.1 become,

$$0 = -\nabla P + j \times B + \rho g \tag{3.2}$$

Which is the magnetohydrostatic equation. The corona is strongly dominated by the magnetic field, the plasma β parameter, which is the ratio of gas pressure to magnetic pressure, is small compared to unity. Thus any pressure gradient is dominated by Lorentz force, and the equation 3.2 reduces to,

$$j \times B = 0 \tag{3.3}$$

The magnetic field that satisfies above equation is called the force-free field, which implies that magnetic field and current density (j) are parallel to each other. Force free field satisfies the following equations.

$$j \times B = 0 \tag{3.4}$$

$$\mu_0 j = \alpha B \tag{3.5}$$

$$\nabla \times B = \mu_0 j \tag{3.6}$$

$$\nabla . B = 0 \tag{3.7}$$

Equation 3.5 is derived from force-free condition, here α is the force free parameter. Equation 3.6 is the Amperes law where μ_0 is the magnetic permeability in vacuum and equation 3.7 is the divergence free condition. Using equation 3.5 and 3.6 we can write,

$$\nabla \times B = \alpha B \tag{3.8}$$

Taking divergence on both side of the equation yield,

$$B . \nabla \alpha = 0 \tag{3.9}$$

Which implies that the value of α is constant along the magnetic field lines. But it may vary from one field line to another.

Mainly there are three different type of extrapolation technique based on the values of α. The simplest method is the potential field extrapolation, where the current density vanishes everywhere. The second method is the linear force-free (LFF) extrapolation, in which the field

lines takes the constant value of the force-free parameter. The third method is the non-linear force-free (NLFF) extrapolation, where the value of α is a function of space. Unlike potential and linear force-free field, numerical techniques are necessary to solve the NLLFF field. The theoretical background for each method is explained in the next section.

3.2 Methods

3.2.1 Potential Field Extrapolation

The Magnetic field that satisfies the following condition is known as potential field or current free field.

$$\nabla \times B = 0 \tag{3.10}$$

Taking the divergence of equation 3.10 and using divergence free condition gives,

$$\nabla^2 B = 0 \tag{3.11}$$

which tells us that the potential field satisfies the Laplacian equation. From equation 3.10, it is clear that the potential field can be written as a gradient of scalar potential (Φ) which satisfies the Laplacian equation.

$$B = \nabla\Phi \tag{3.12}$$

$$\nabla^2\Phi = 0 \tag{3.13}$$

This is a Neumann boundary value problem for which a unique solution is guaranteed. Once Φ is found the field component can be calculated using equation 3.12. The solution of this equation is easy to compute, only requires the normal component of magnetic field at the lower boundary. The potential field can be calculated using Green functions [16], and Fourier transform technique [17, 18] either in Cartesian or spherical coordinates. As compared to green function method Fourier transform method is computationally easier, takes only less amount of time depending on the size of the region of interest. The Fourier method is explained below.

First we have chosen a Cartesian coordinate system with positive z-axis towards the observer. The z = 0 plane represent the photosphere of the sun, where the magnetic field measurement available. The general solution to equation 3.12 and 3.13 that decays to zero as z tends to infinity and is periodic in x and y plane has the form,

$$\Phi = \Phi_k \times exp(ik_x x + ik_y y - kz) \tag{3.14}$$

Where k_x, k_y are real and $k^2 = k_x^2 + k_y^2$ and Φ_k is unknown constant. The solution is obtained by the method of separation of variable. If the magnetic field vanishes at the side planes x=0, x=a,

y=0, y=b, the general solution is [15],

$$\Phi = \sum_{n=0}^{\infty}\sum_{m=0}^{\infty} \Phi_{nm} sin(\frac{2n\pi x}{a}) sin(\frac{2m\pi y}{a}) exp(-k_{nm} z) \tag{3.15}$$

In spherical polar coordinate (r, θ, ϕ) the general solution to Laplacian equation is,

$$\Phi = \sum_{l=0}^{\infty}\sum_{m=-l}^{l} [a_{lm} r^l + b_l r^{-(l+1)}] P_l^m(cos\theta) exp(im\phi) \tag{3.16}$$

Where $P_l^m(cos\theta)$ is the associated Legendre polynomial. The unknown constant in general solution can be computed by applying boundary condition. The magnetic field values ($B_z(x, y, z = 0)$) over a given rectangular domain are known from photospheric magnetogram. Thus ($B_z(x, y, z = 0)$) can be used as a boundary condition to calculate magnetic field values above photosphere ($B(x, y, z)$). The value of Φ_k in equation 3.14 is calculated using equation 3.12 at z=0 plane, which yield, [18]

$$B_z(x, y, z = 0) = \sum_{k_x}\sum_{k_y} -k\Phi_k exp(ik_x + ik_y) \tag{3.17}$$

Or taking Fourier transform gives,

$$-k\Phi_k = \sum_{k_x}\sum_{k_y} B_z(x, y, z = 0) exp(-ik_x - ik_y) \tag{3.18}$$

$$= B_z(k) \tag{3.19}$$

$B_z(k)$ is the two dimensional Fourier transform of $B_z(x, y, z = 0)$. From equation 3.18 and 3.19,

$$\Phi_k = \frac{-1}{k} B_z(k) \tag{3.20}$$

3.2.2 Linear Force-Free Extrapolation

The magnetic field that satisfies the following equation is known as Linear force-free field.

$$\nabla \times B = \alpha B \tag{3.21}$$

Where α is a constant along the field lines and it does not change from one field line to another. Taking curl on equation 3.21 and using divergence free condition gives,

$$(\nabla^2 + \alpha^2) B = 0 \tag{3.22}$$

Thus linear force free field satisfies the Helmholtz equation. Using poloidal and toroidal decomposition magnetic field can be written in terms of two scalar functions [19],

$$B = \nabla \times Tz + \nabla \times \nabla \times Pz \tag{3.23}$$

Where z is some constant vector. T and P are the toroidal and poloidal scalar respectively. Relation between scalar function T and P are shown below.

$$T = \alpha P \tag{3.24}$$

Thus it can be easily shown that poloidal scalar also satisfies the Helmholtz equation.

$$(\nabla^2 + \alpha^2)P = 0 \tag{3.25}$$

The numerical techniques to solve this linear problem are the Green function [20, 21], vertical integration [22], Fourier expansion [17] methods in Cartesian and spherical coordinates. The Cartesian coordinate system chosen here has positive z-axis directing towards the observer and z=0 plane on the surface (photosphere) of the Sun. The general solution to equation 3.24 and 3.25 that decays to zero as z tends to infinity and periodic in x and y has the form,

$$P(x,y,z) = \sum_{k_x}\sum_{k_y} P_k exp(ik_x x + ik_y y - (k_x^2 + k_y^2 - \alpha^2)z) \tag{3.26}$$

Where k_x and k_y are real. P_k is an unknown constant which can be computed using the boundary condition. The solution is computed using the method of separation of variable. General solution to linear force free field in spherical coordinate(r,θ,ϕ) is shown below [15].

$$P(r,\theta,\phi) = \sum_{n=0}^{\infty}\sum_{m=0}^{\infty} A_{nm} J_{n+1/2}(\alpha r) P_n^m(cos\theta) exp(im\phi) \tag{3.27}$$

where $P_n^m(cos\theta)$ is the associated Legendre polynomial and $J_{n+\frac{1}{2}}$ is the spherical Bessel function of order $n+\frac{1}{2}$. A_{nm} is a complex constant.

The value of P_k in equation 3.26 is calculated by including boundary condition. The boundary condition here is the horizontal distribution of the line of sight component of of magnetic field measured at photospheric height ($B_z(x,y,z=0)$). From equation 3.23 the value of LOS component of field is given below.

$$B_z(x,y,z) = -\frac{\partial^2 P}{\partial^2 x} - \frac{\partial^2 P}{\partial^2 y} \tag{3.28}$$

Applying equation 3.28 on 3.26 at z=0 gives, [18]

$$B(x,y,z=0) = \sum_{k_x}\sum_{k_y} (k_x^2 + k_y^2) P_k exp(ik_x x + ik_y y) \tag{3.29}$$

Or taking Fourier transform

$$(k_x^2 + k_y^2)P_k = \sum_{k_x}\sum_{k_y} B(x,y,z=0)exp(-ik_x x - ik_y y) \tag{3.30}$$

$$= B_z(k) \tag{3.31}$$

$B_z(k)$ is the two dimensional Fourier transform of observed line of sight magnetic field. From equation 3.30 and 3.29 we can write,

$$P_k = \frac{B_z(k)}{k_x^2 + k_y^2} \tag{3.32}$$

By substituting equation 3.32 in general solution the value of P can be obtained. But the problem here is the value of α, it can only be obtained from vector magnetogram.

$$\alpha = \frac{1}{B_z}\left(\frac{\partial B_y}{\partial x} - \frac{\partial B_x}{\partial y}\right) \tag{3.33}$$

The above equation is used to create the α map of the region of interest and used the average value of α as an input in equation 3.29.

3.2.3 Non-Linear Force-Free Extrapolation

Potential and linear force-free field can be used as a first step to model solar corona. They are the solution to an oversimplified underlying mathematical problem. The actual problem is non-linear, we linearised the equation to reduce mathematical difficulty in solving the equation. So the potential and linear force-free field, which are based on linearised equation cannot represent the real physical situation. Also, the value of α in an active region is a strong function of space; we found this in deriving α map from equation 3.33. From these arguments, it is clear that force-free models are necessary to reconstruct the coronal magnetic field.

$$\nabla \times B = \alpha(r)B \tag{3.34}$$

The field that satisfies the above condition is known as the non-linear force-free field. For the non-linear force-free field the α value varies from one field line to another [23]. Solving above equation is a difficult task, analytic techniques cannot be used due to the non-linearity of the equation. So we have to use the numerical technique to solve the problem. Semi-analytic solution to equation 3.34 can be calculated assuming axis symmetric magnetic field [24]. In spherical polar coordinate axis-symmetric magnetic field can be expressed as

$$B = \frac{1}{rsin\theta}\left(\frac{1}{r}\frac{\partial A}{\partial \theta}\hat{r} - \frac{\partial A}{\partial r}\hat{\theta} + Q\hat{\phi}\right) \tag{3.35}$$

Where A is the flux function and Q is strict function of A with

$$\alpha = \frac{dQ}{dA} \tag{3.36}$$

$$0 = \frac{\partial^2 A}{\partial r^2} + \frac{1-\mu^2}{r^2}\frac{\partial^2 A}{\partial \mu^2} + Q\frac{dQ}{dA} \tag{3.37}$$

Where $\mu = cos\theta$. Equation 3.37 is the Grad-Shafranov equation, and its separable solutions are,

$$A = P(\mu)r^n \tag{3.38}$$

$$Q(A) = aA^{1+1/n} \tag{3.39}$$

Where a and n are constants. Substituting equation 3.38 and 3.39 in 3.37 gives,

$$0 = (1-\mu^2)\frac{d^2P}{d\mu^2} + n(n+1)P + a^2\frac{1+n}{n}P^{1+2/n} \tag{3.40}$$

The boundary condition applied here are, the magnetic field will go to zero for very large values of r and B_θ and B_ϕ vanish along the axis μ =1, -1. These conditions yield,

$$P = 0 \qquad at \quad \mu = 1, -1 \tag{3.41}$$

Solution to non linear differential equation 3.40 with boundary condition given by equation 3.41 will generate non linear force free field. Only some particular values of n and a can lead to the solution of equation 3.40 that satisfies the boundary condition. This is an eigenvalue problem, so technique like shooting method can be used to generate the solution. Semi analytic solution to non linear force free fields developed by B.C.Low and Lou are now used for testing various NLFF extrapolation methods.

Two main technique used for NLFF extrapolation are the optimization [23] method and Aschwanden code [28]. Optimization procedure need vector magnetogram as input, but for Aschwanden code which is based on vertical current approximation to extrapolate magnetic field from photospheric LOS magnetogram. In the following section we will explain the theoretical background behind these methods.

Optimization Method

Optimization method involves the minimisation of the quantity

$$L = \int_V [B^{-2}|(\nabla \times B) \times B|^2 + |\nabla . B|^2] dV \tag{3.42}$$

by an evolutionary procedure [25]. Reducing the value of L to zero implies that,

$$(\nabla \times B) \times B = 0 \tag{3.43}$$

$$\nabla . B = 0 \tag{3.44}$$

in the volume V. Thus a force free field is obtained by minimising the quantity L. Differentiating L with respect to iteration parameter t and applying a number of vector identity yield,

$$\frac{1}{2}\frac{dL}{dt} = -\int_V \frac{\partial B}{\partial t}.F dV - \int_S \frac{\partial B}{\partial t}.G dS \tag{3.45}$$

where

$$F = \nabla \times (\Omega \times B) - \Omega \times (\nabla \times B) - \nabla(\Omega.B) + \Omega(\nabla.B) + \Omega^2 B \tag{3.46}$$

$$G = \hat{n} \times (\Omega \times B) - \hat{n}(\Omega.B) \tag{3.47}$$

$$\Omega = B^{-2}[(\nabla \times) \times B - (\nabla.B)B] \tag{3.48}$$

Here S is a surface bounding the volume V and $\hat{n}$ is the normal unit vector pointing towards the interior of the surface. The detailed derivation of these quantities are shown in [25]. From equation 3.45 it is clear that the value of L will decrease if we choose following conditions.

$$\frac{\partial B}{\partial t} = \mu F \tag{3.49}$$

$$\frac{\partial B}{\partial t} = 0 \qquad on\ the\ surface\ S \tag{3.50}$$

μ in equation 3.49 is an arbitrary function which is greater than zero and it helps to speed up the convergence of iteration step. Applying equation 3.49 and 3.50 in 3.45 gives,

$$\frac{\partial B}{\partial t} = -\mu F^2 \tag{3.51}$$

One of the problems with this optimization method is that all three components of the magnetic field have to be prescribed on the six boundaries of the computational box. This complication is arrived from equation 3.50. Magnetic field values at the lower boundary are already known from photospheric vector magnetogram. For the remaining five boundaries, we have to use potential or linear force-free extrapolation method to calculate all components magnetic field. Another issue with this procedure is that the quantity L may not necessarily be reduced to zero, or close to zero. In this case, the field inside the volume is not force-free and does not satisfy the divergence-free condition. This difficulty arrives from the force-free assumption, where we assumed that photosphere is also force-free. Solar photosphere is not in a force-free condition [26]. So force-free extrapolation from photospheric magnetogram is not a good way reconstruct the coronal field. One way to overcome this problem is to preprocess the photospheric vector magnetic field data. The detailed description preprocessing routine is

shown in [27]. The method involves the minimisation of the quantity

$$L = \mu_1 L_1 + \mu_2 L_2 + \mu_3 L_3 + \mu_4 L_4 \tag{3.52}$$

where

$$L_1 = \left[\left(\sum_p B_x B_z \right)^2 + \left(\sum_p B_y B_z \right)^2 + \left(\sum_p B_z^2 - B_x^2 - B_y^2 \right)^2 \right] \tag{3.53}$$

$$L_2 = \left[\left(\sum_p x(B_z^2 - B_x^2 - B_y^2) \right)^2 + \left(\sum_p y(B_z^2 - B_x^2 - B_y^2) \right)^2 + \left(\sum_p y B_x B_z - x B_y B_Z \right)^2 \right] \tag{3.54}$$

$$L_3 = \left[\sum_p (B_x - B_{xobs})^2 + \sum_p (B_y - B_{yobs})^2 + \sum_p (B_z - B_{zobs})^2 \right] \tag{3.55}$$

$$L_4 = \left[\sum_p (\nabla B_x)^2 + (\nabla B_y)^2 + (\nabla B_z)^2 \right] \tag{3.56}$$

Here the summation is over entire pixels p of the photospheric magnetogram. Minimisation of the quantity L_1 and L_2 leads to vanishing of total force and torque on the lower boundary respectively. The preprocessed magnetogram cannot deviate largely from the observed one, this is taken care by minimisation of L_3. The term L_4 controlls the smoothing. Simultaneous minimisation of the above terms will give magnetogram that satisfies the force free condition.

Non-Linear Force-Free Code by Vertical Current Approximation

Uni polar magnetic charges that are buried below the solar surface is a simple example of the potential field which satisfies Maxwell's divergence-free condition [28]. Thus potential field in the region of interest can be constructed by the superposition of n_{mag} uni-polar magnetic charges. Theoretical construction of field is done in a Cartesian coordinate system, where the origin is at the centre of the Sun. The magnetic field at arbitrary location **x**=(x, y, z) in corona which falls with the square of the distance is given by [28],

$$B(\mathbf{x}) = \sum_{m=1}^{n_{mag}} B_m \left(\frac{d_m}{r_m} \right)^2 \frac{\mathbf{r}_m}{r_m} \tag{3.57}$$

Where B_m is the magnetic field strength at the solar surface(photosphere) above m^{th} buried charge. r_m is the distance between location of the buried charge(x_m, y_m, z_m) and arbitrary location in corona. d_m represents the depth of the magnetic charge,

$$d_m = 1 - \sqrt{x_m^2 + y_m^2 + z_m^2} \tag{3.58}$$

Potential field is parameterized by four quantities B_z, x_m, y_m, z_m. The location and the strength of magnetic charges are unknown; this can be computed using an iterative method using photospheric magnetogram (see [28, 29]). Once we know all four parameters, the volume

filling potential field is generated using equation 3.57. We aim to generate the non-linear force-free field (NLFFF) in 3-dimensional space; this is done by introducing vertical current above magnetic charges. Now the magnetic field is not potential because vertical current adds an azimuthal magnetic field component, which introduces twist around the vertical axis. The solution for a twisted field of magnetic charge in the spherical coordinate system is obtained by comparing the exact analytical solution for uniformly twisted flux tube in cylindrical geometry [15]. This was done using coordinate transformation. Solutions are given below,

$$B_r(r,\theta) = B_0 \left(\frac{d^2}{r^2}\right) \frac{1}{(1+b^2r^2sin^2\theta)} \tag{3.59}$$

$$B_\phi(r,\theta) = B_0 \left(\frac{d^2}{r^2}\right) \frac{brsin\theta}{(1+b^2r^2sin^2\theta)} \tag{3.60}$$

$$B_\theta(r,\theta) = 0 \tag{3.61}$$

$$\alpha(r,\theta = \frac{2bcos\theta}{(1+b^2r^2sin^2\theta)}) \tag{3.62}$$

where

$$b = \frac{2\pi n_{twist}}{l} \tag{3.63}$$

which represent the number of full twisting turn n_{twist}over loop length l. $B_r(r,\theta)$ is the radial potential potential field component and $B_\phi(r,\theta)$ is the azimuthal non potential component. α in equation 3.62 is the force free parameter, which reduces to zero in the limit of vanishing twist. Like potential field space filling non potential field at any arbitrary location in corona $\mathbf{x} = (x,y,z)$ can be represented by the superposition of n_{mag} magnetic charges.

$$\mathbf{B}^{np}(\mathbf{x}) = \sum_{m=1}^{n_{mag}} \mathbf{B}_m^{np}(\mathbf{x}) \tag{3.64}$$

Once we know parameter B_z, x_m, y_m, z_m, α_m for each buried magnetic charges, the space filling non linear force free field can be generated. First four parameter are already obtained in potential field calculation and the α_m for each charge is computed by iterative procedure. The main advantage of this code is that, it uses observed intensity images to track the loop coordinate. So it is a steroscopically constrained magnetic modelling. The main task of NLFFF code is to calculate non-potential parameter (α_m) for each buried magnetic charges by minimising the misalignment angle between theoretical magnetic model (B^{theo}) and observed loop direction (B^{obs}) [28]. 3D miss-alignment angle is defined as,

$$\mu_3 = cos^{-1}\left(\frac{(\mathbf{B}^{theo}.\mathbf{B}^{obs})}{|\mathbf{B}^{theo}|.|\mathbf{B}^{obs}|}\right) \tag{3.65}$$

3.3 Results and Discussion

3.3.1 Potential field extrapolation

Magnetic field map of an active region generated using the potential field extrapolation method are shown figure 3.1. Each image represents different height in the solar atmosphere. Figure 3.1(a) is the line of sight magnetogram observed by HMI onboard SDO. The magnetic field is then extrapolated to different height in solar atmosphere from photospheric LOS magnetogram. LOS component of extrapolated field at height 5, 19 px are shown in figure 3.1 (b), (c) respectively. Here 1 px represents 362.5 km height above the photosphere. Here we can see that the field strength decreases with height, that is expected from potential field solution. But one problem here is that the field is getting diffused as height increases.

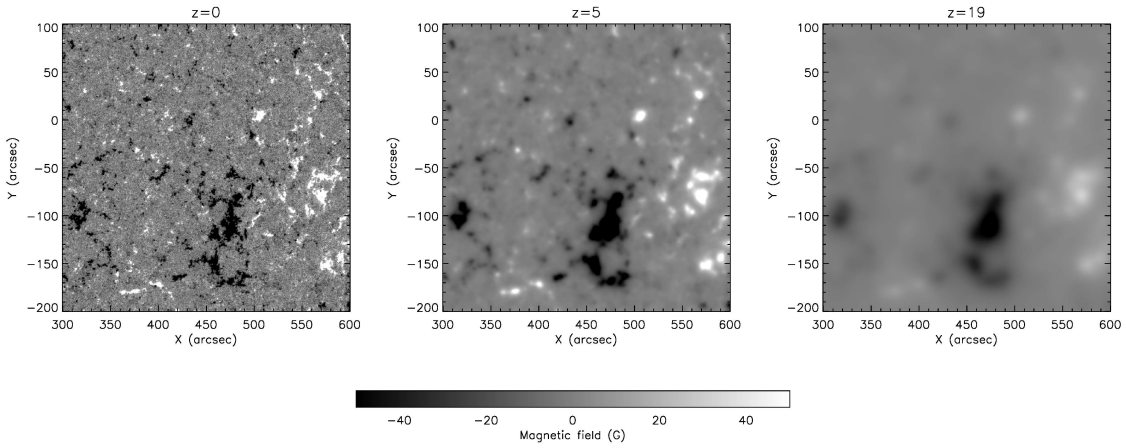

Figure 3.1: Potential field extrapolation. (a): Photospheric LOS magnetogram (b): LOS component of extrapolated magnetic field map at height z= 5 px. (c): LOS component of extrapolated magnetic field map at height z= 19 px

3.3.2 Linear force-free field extrapolation

Figure 3.2 displays the magnetic field map of an active region generated using the linear force-free extrapolation method. The left panel shows the x, y, z component map of photospheric magnetic field observed by HMI and the corresponding extrapolated field maps at height z=10 px are shown in right panel. As mentioned before 1 px corresponds to 362.5 km height above the photosphere. The value of force-free parameter α is necessary to calculate linear force-free field, this is the only reason, why vector magnetogram is needed in linear force-free field computation. The computed α value was 0.03 which is very close zero. From Figure 3.2 it is clear that the field is getting diffused as height increases. Also, the strength of the field decreases with height. If the non-linearity in the active region is less, then the linear force-free extrapolation is a good way to reconstruct the coronal magnetic field.

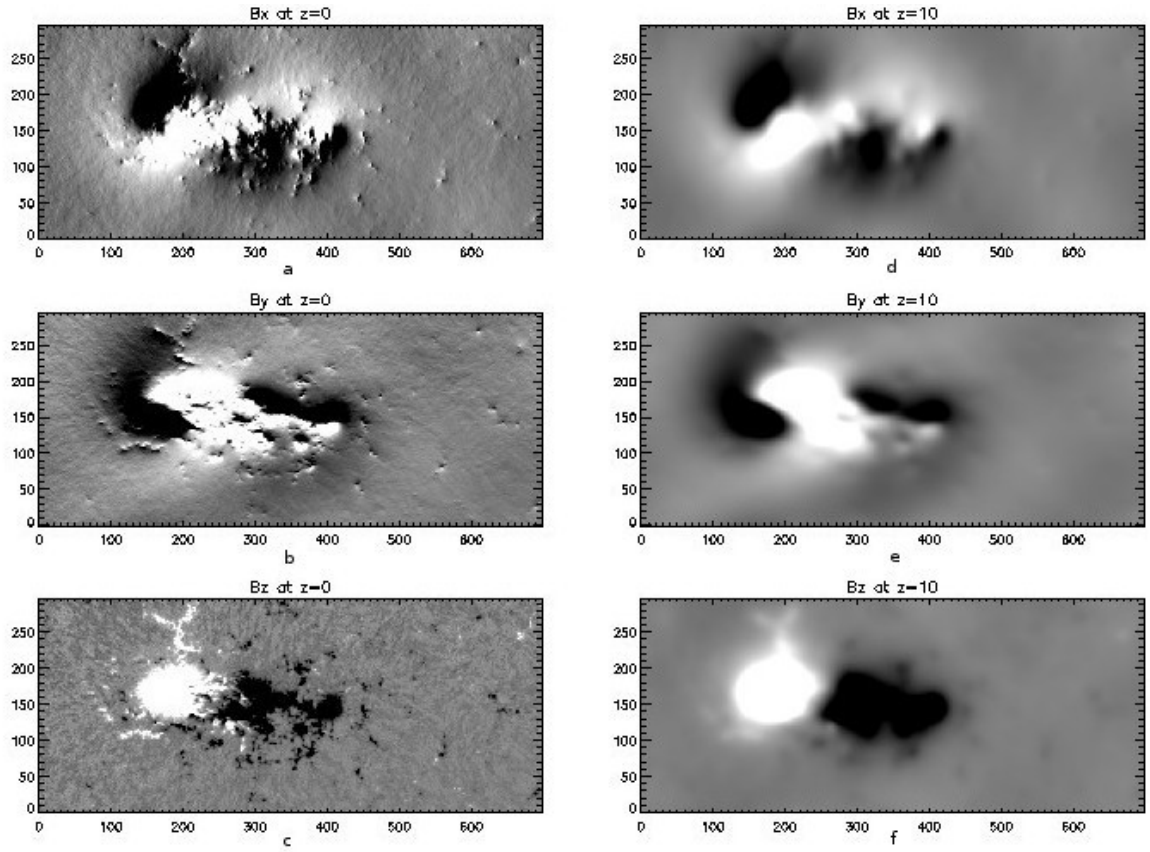

Figure 3.2: Linear force free field extrapolation. (a): x component of photospheric magnetic field (b): y component of photospheric magnetic field (c): Photospheric LOS magnetogram. (d): x component of extrapolated field at height z=10 px. (e): y component of extrapolated field at height z=10 px. (f): LOS component of extrapolated field at height z=10 px

3.3.3 Non-linear force-free extrapolation

Optimization method

3D magnetic field model of a coronal hole generated using Wiegelmann's optimization procedure is displayed in figure 3.3. The yellow line represents the magnetic field line, and the bottom boundary is the LOS magnetogram. First, the magnetic field data was preprocessed to make it force free at the photosphere. Flux balancing of observed magnetogram was carried out by adding an extra layer of pixels around it. To perform optimization, it is necessary to know the magnetic field values on the six boundaries of the computational box. All 3 component of the field on the lower boundary is already known from photospheric vector magnetogram; here the remaining five are calculated using potential field extrapolation.

NLFF code using vertical current approximation

We performed magnetic modelling for the active region NOAA 12230 using the NLFFF code that is based on vertical current approximation. The magnetic field of this particular active region was represented by the superposition of 200 uni-polar magnetic sources (n_{mag}). This

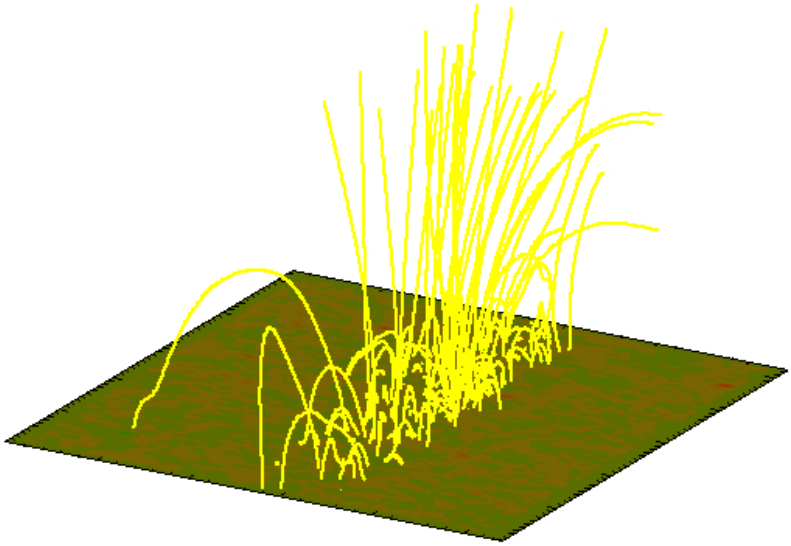

Figure 3.3: Magnetic modelling of the coronal hole using optimization method

specific value of n_{mag} depends on the topological complexity of the magnetic field in the active region and the field of view (0.35 $\times$ .35 solar radii). The detection of coronal loops is performed only using AIA 193 $\mathring{A}$ and 171 $\mathring{A}$ channel images. The automated tracing of loop coordinate is carried out by the method of Oriented Coronal Curved Loop Tracing (OCCULT-2) (Aschwanden 2013 a). The code then performs the task that fits the nonlinear force-free solution to the geometry of the traced loops, by minimising the 3D misalignment angle, which is done by the sufficient number of iteration steps. The minimum number of iteration (n_{itmin}) used here was 30, and we set the maximum number of iteration (n_{itmax}) at 100.

The result of non-linear force-free magnetic field extrapolation of NOAA 12230 data corresponds to 2014 December 12, 19:30 UT is shown in figure 3.4. The upper left image shows the 3D loop trajectories, and the field lines and the lower left represent the 2D line of sight view of the field line overlaid on HMI LOS magnetogram. In each image, the red line represents magnetic field line, and yellow represents the observed loops. Magnetic field lines shown in these images are the field line which intersects the midpoint of traced loop segments. Various input parameters used for codes and output parameters obtained are shown in right panel. The extrapolated magnetic field lines of active region NOAA 12230 observed on 2014/12/12 at 19:30 UT overlaid on 171 $\mathring{A}$ image are shown in figure 3.5. The field lines are shown in red colour. We selected a rectangular grid of foot points in a 20 x 20 grid with minimum magnetic field strength 50 Gauss. This image showed an excellent co-alignment between observed loops and extrapolated magnetic field lines, which proves the success of NLLFF extrapolation method. But there were few field lines that are not aligned with obsreved loop structures.

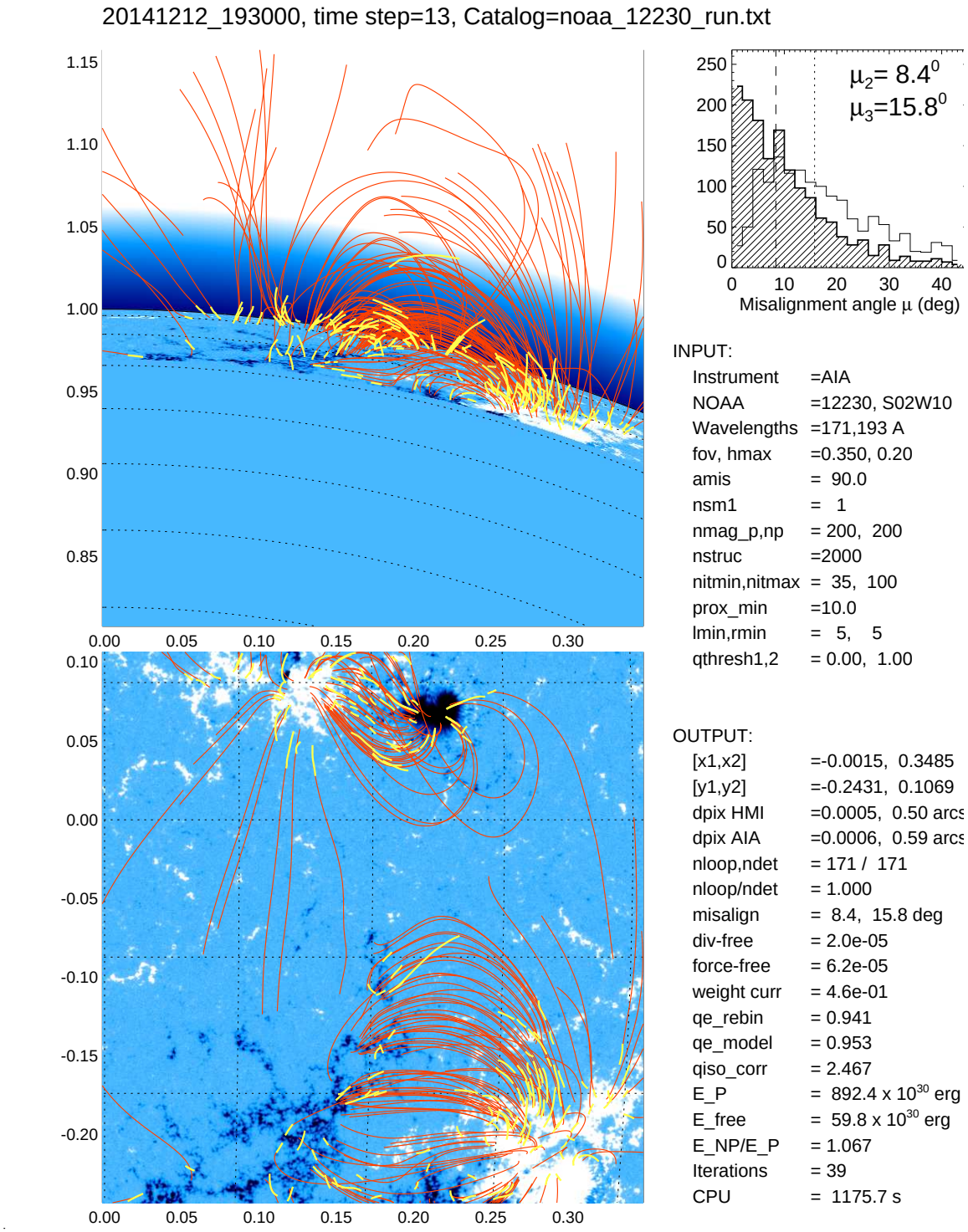

Figure 3.4: NLFF modelling of active region NOAA-12230 by vertical current approximation.

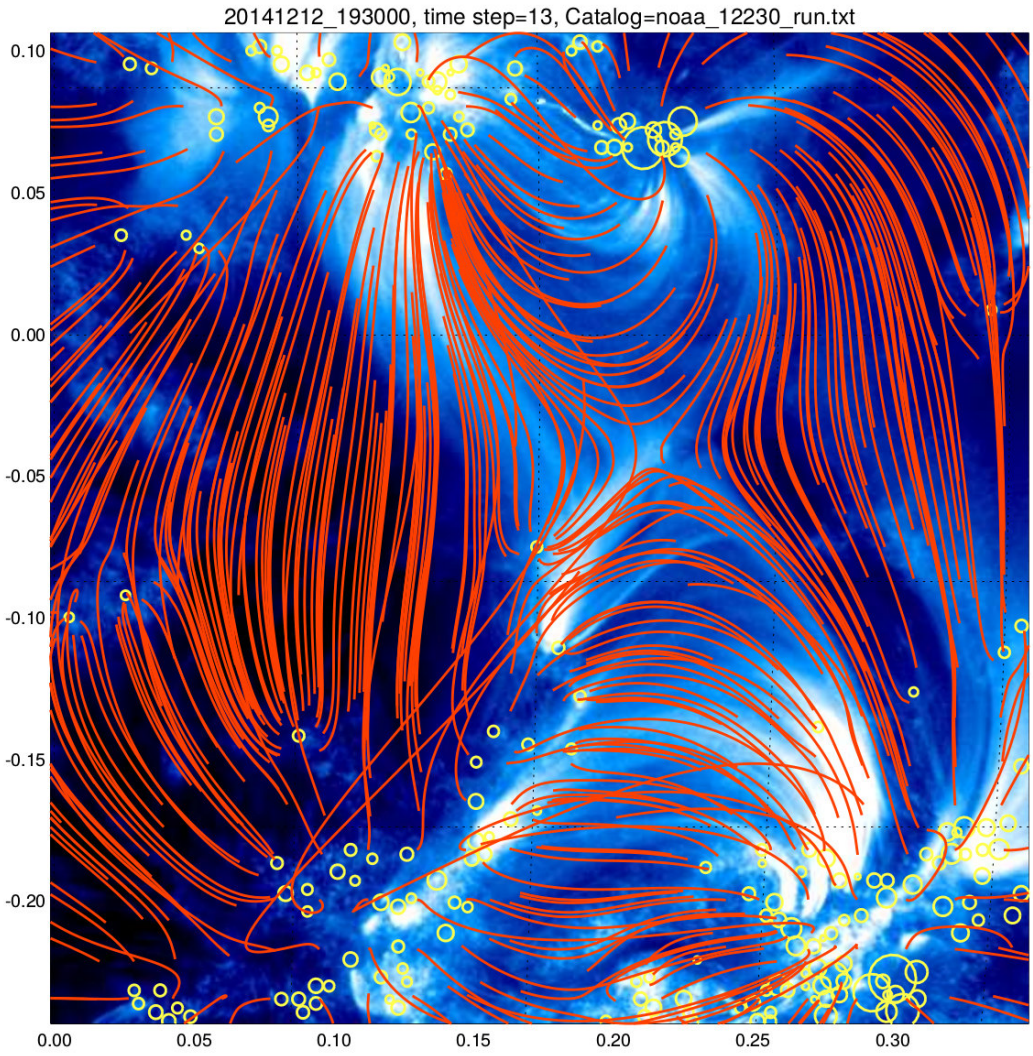

Figure 3.5: Non linear force free extrapolation: Extrapolated magnetic field lines of active region NOAA 12230 observed on 2014/12/12 at 19:30 UT overlaid on 171 $\AA$ image

3.4 Conclusions

Most of the phenomenon occurring on the Sun are driven by the magnetic field, it connects the interior of the Sun with its atmosphere. So the accurate measurement of the magnetic field is crucial to understand the Sun. Recent mission HMI onboard SDO and various ground-based telescopes provide high-resolution magnetograms. These measurements are only possible at photospheric height. To measure coronal magnetic field, extrapolation techniques are required. The potential and linear force-free field can be used as the first step to model coronal structure. But these methods are developed from, linearising the underlying non-linear mathematical problem. Thus non-linear force-free extrapolation methods are necessary to model coronal structure.

Different NLFF codes have been proposed, to compute coronal magnetic field from photo-

spheric magnetogram. The problem here is that the photosphere is not force-free. Extrapolation of the force-free field from a non-force-free boundary condition is not correct. Another problem is about the accuracy of photospheric magnetic field measurement. Compared to LOS component of the field the measurement of the transverse component is less accurate. All these problems have to be taken into account before extrapolating from the photospheric data. Preprocessing the magnetogram is the best way to avoid these problems, which is done using Wigelmann's optimization procedure. One of the well known NLFF code is Aschwanden code which is based on the vertical current approximation. This method deconvolves the line of sight magnetogram into a specified number of potential field magnetic sources, and the non-potential field is constructed by introducing a vertical current above magnetic charges. The primary task of NLFFF code is to calculate non-potential parameter (α_m) for each buried magnetic charges by minimising the misalignment angle (μ_3). Inclusion stereoscopic data in force-free modelling is the main advantage of the Aschwanden code over optimization procedure. Compared to Aschwanden code optimization procedure is computationally complicated and far too time-consuming.

Magnetic field is responsible for the loop-like structures in the solar atmosphere. From the results Aschwanden code we have seen that there is good co-alignment between loop structure and extrapolated field lines. This proves that NLFF code based on vertical current approximation is a right way to reconstruct the coronal force-free field despite some differences in the observed and extrapolated field.

Having understood the QS and CH as well as extrapolation techniques, we shall perform the extrapolations in QS and CH using the data from HMI and study the differences.

Bibliography

[1] Grandpierre, A., *A pulsating-ejecting solar core model and the solar neutrino problem.*, Astronomy and Astrophysics **308**, 199-212 (1996).

[2] Shu, Frank, *The physical universe: an introduction to astronomy* (University science books, 1982).

[3] Mariska, John T, *The solar transition region* (Cambridge University Press, UK, 1992).

[4] Munro, R. H. and Withbroe, G. L, *Properties of a Coronal Hole from EUV Observations*, Bulletin of the American Astronomical Society **4**, 388 (1972).

[5] Malanushenko, O. V. and Jones, H. P, *Differentiating Coronal Holes from the Quiet Sun by He 1083 nm imaging spectroscopy*, Bulletin of the American Astronomical Society **36**, 797 (2004).

[6] Howard, R., *Large-scale solar magnetic fields*, Annual Review of Astron and Astrophys **15**, 153-173 (1977).

[7] Wiegelmann, T. and Solanki, S. K., *Similarities and Differences between Coronal Holes and the Quiet Sun: Are Loop Statistics the Key?*, solphys **225**, 227-247 (2004).

[8] De Pontieu, B. and Title, A. M. and Lemen, J. and Wuelser, J. and Tarbell, T. D. and Schrijver, C. J. and Golub, L. and Kankelborg, C. and Carlsson, M. and Hansteen, V. H. and Worden, S. and IRIS Team, *The Interface Region Imaging Spectrograph (IRIS)*, Solar Physics Division Abstracts **44**, 100.03 (2013).

[9] Huang, Z. and Madjarska, M. S. and Scullion, E. M. and Xia, L.-D. and Doyle, J. G. and Ray, T., *Explosive events in active region observed by IRIS and SST/CRISP*, Monthly Notices of the Royal Astronomical Society (MNRAS) **464**, 1753-1761 (2017).

[10] Sandlin, G. D. and Bartoe, J.-D. F. and Brueckner, G. E. and Tousey, R. and Vanhoosier, M. E., *The high-resolution solar spectrum, 1175-1710 A*, Astrophysical Journal Supplement **61**, 801-898 (1986).

[11] McIntosh, S. W., de Pontieu, B., Hansteen, V., Carlsson, M., and Boerner, P, *A User's Guide toIRIS Data Retrieval, Reduction and Analysis*, 2014 , ().

[12] Tadesse, T. and Wiegelmann, T. and Inhester, B. and MacNeice, P. and Pevtsov, A. and Sun, X., *Full-disk nonlinear force-free field extrapolation of SDO/HMI and SOLIS/VSM magnetograms*, Astronomy and Astrophysics **550**, A14 (2013).

[13] Centeno, R. and Schou, J. and Hayashi, K. and Norton, A. and Hoeksema, J. T. and Liu, Y. and Leka, K. D. and Barnes, G., *The Helioseismic and Magnetic Imager (HMI) Vector Magnetic Field Pipeline: Optimization of the Spectral Line Inversion Code*, Solar Physics **289**, 3531-3547 (2014).

[14] Vemareddy, P. and Ambastha, A. and Wiegelmann, T., *Magnetic structure of solar active region NOAA 11158*, Bulletin of the Astronomical Society of India **41**, 183 (2013).

[15] Priest, E., *Magnetohydrodynamics of the Sun* (Cambridge University Press, UK, 2014).

[16] Sakurai, T., *Green's Function Methods for Potential Magnetic Fields*, Solar Physics **76**, 301-321 (1982).

[17] Nakagawa, Y. and Raadu, M. A., *On Practical Representation of Magnetic Field*, Solar Physics **25**, 127-135 (1972).

[18] Levine, R. H. and Altschuler, M. D., *Representations of coronal magnetic fields including currents*, Solar Physics **36**, 345-350 (1974).

[19] Chandrasekhar S., *Hydrodynamic and Hydrodynamic stability* (Oxford University Press, UK, 1961).

[20] Semel, M., *Extrapolation functions for constant-alpha force-free fields - Green's method for the oblique boundary value*, Astronomy and Astrophysics **198**, 293-299 (1988).

[21] Chiu, Y. T. and Hilton, H. H., *Exact Green's function method of solar force-free magnetic-field computations with constant alpha. I - Theory and basic test cases*, Astrophysical Journal **212**, 873-885 (1977).

[22] Amari, T. and Boulmezaoud, T. Z. and Maday, Y., *A regularization method for the extrapolationbreak of the photospheric solar magnetic field. I. Linear force-free field*, Astronomy and Astrophysics **339**, 252-260 (1998).

[23] Wiegelmann, T., *Nonlinear force-free modeling of the solar coronal magnetic field*, Journal of Geophysical Research (Space Physics) **113**, A03S02 (2008).

[24] Low, B. C. and Lou, Y. Q., *Modeling solar force-free magnetic fields*, Astrophysical Journal **352**, 343-352 (1990).

[25] Wheatland, M. S. and Sturrock, P. A. and Roumeliotis, G., *An Optimization Approach to Reconstructing Force-free Fields*, Astrophysical Journal **540**, 1150-1155 (2000).

[26] Metcalf, T. R. and Jiao, L. and McClymont, A. N. and Canfield, R. C. and Uitenbroek, H., *Is the solar chromospheric magnetic field force-free?*, Astrophysical Journal **439**, 474-481 (1995).

[27] Wiegelmann, T. and Inhester, B. and Sakurai, T., *Preprocessing of Vector Magnetograph Data for a Nonlinear Force-Free Magnetic Field Reconstruction*, Solar Physics **233**, 215-232 (2006).

[28] Aschwanden, M. J., *The Vertical-current Approximation Nonlinear Force-free Field Code- Description, Performance Tests, and Measurements of Magnetic Energies Dissipated in Solar Flares*, Astrophysical Journal ,Supplement **224**, 25 (2016).

[29] Aschwanden, M. J. and Wuelser, J.-P. and Nitta, N. V. and Lemen, J. R. and DeRosa, M. L. and Malanushenko, A., *First Three-dimensional Reconstructions of Coronal Loops with the STEREO A+B Spacecraft. IV. Magnetic Modeling with Twisted Force-free Fields*, Astrophysical Journal **756**, 124 (2012).